Letter Vol. 45, No. 17 / 1 September 2020 / *Optics Letters* 4935

Optics Letters

Infrared properties of high-purity silicon

Edward J. Wollack,* **Giuseppe Cataldo, Kevin H. Miller,** and **Manuel A. Quijada**

NASA Goddard Space Flight Center, 8800 Greenbelt Road, Greenbelt, Maryland 20771, USA
**Corresponding author: Edward.J.Wollack@NASA.gov*

Received 27 March 2020; revised 31 July 2020; accepted 1 August 2020; posted 3 August 2020 (Doc. ID 393847); published 31 August 2020

High-purity silicon is a readily available material of utility in realizing a variety of long-wavelength optical and guided wave components. The transmittance of uncompensated for silicon is measured in the far- and mid-infrared regimes at room and cryogenic temperatures. The experimental and analysis techniques used to extract the refractive index from $100-1000\ \mathrm{cm}^{-1}$ (100–10 μm) are presented, and the results are compared to the literature. An average refractive index below $300\ \mathrm{cm}^{-1}$, $\hat{n}(300\ \mathrm{K}) = 3.417 + i\,8.9 \times 10^{-5}$, which transitions in cooling to $\hat{n}(10\ \mathrm{K}) = 3.389 + i\,4.9 \times 10^{-6}$, is observed.

https://doi.org/10.1364/OL.393847

Silicon has found utility in the far infrared due to its low loss, radiation tolerance, insulating properties, and general compatibility with optical coating and micro-fabrication processing. These properties have led to its widespread use in electronic [1] as well as optical [2,3] and detector applications at cryogenic temperatures [4,5]. As a semiconductor, the performance of silicon in these settings is a function of temperature, photo-illumination energy [6], and defect concentration [7,8]. Processing details such as compensated for doping [9], irradiation induced defects [10–12], and thermal donor annihilation [13] are also observed to influence silicon's long-wavelength absorption characteristics. Similarly, relative to p-type material, n-type doped silicon has a lower sensitivity to the presence of dislocations, achieves lower recombination rates [14], and provides a compelling candidate for low-loss infrared applications. Early cryogenic studies of silicon [15–17] concentrated primarily on the multi-phonon absorption response near $400-1400\ \mathrm{cm}^{-1}$.

Here, the infrared properties of bulk silicon are characterized and compared to prior measurements reported in the literature. A high-purity silicon sample with the following material specifications was used in this investigation: uncompensated for silicon with impurity levels of $[\mathrm{C}] < 2 \times 10^{16}\ \mathrm{atoms/cm}^3$ and $[\mathrm{O}] < 1 \times 10^{16}\ \mathrm{atoms/cm}^3$, bulk resistivity $\approx 30-40\ \mathrm{k}\Omega - \mathrm{cm}$, and 2.47 msec carrier lifetime at room temperature (www.topsil.com). A section of this boule was subsequently formed into a right cylinder 25 mm in diameter and 9.907(4) mm thick (i.e., where parentheses indicate measurement accuracy) with opposing optically polished faces maintaining a parallelism <0.2 arc-seconds.

The transmittance of the silicon sample was measured with a Bruker IFS 125 high-resolution Fourier transform spectrometer (FTS) in a collimated beam geometry at physical temperatures of 300 K and 10 K. The silicon sample was mounted in an Oxford dynamic-flow liquid-helium cryostat with polypropylene windows, whose position corresponded to the collimated optical region. A pair of off-axis parabolas matched to the FTS focal number, $\simeq f/6$, were used to define the collimated beam space within the instrument sample chamber. This collimated configuration minimizes differences in illumination and optical alignment encountered by the beam as it propagates through the thick high-index sample versus the reference path used for calibration. The reference and sample positions can be interchanged *in situ* while maintaining the integrity of the instrument's evacuated optical paths. Two combinations of sources, beam splitter and detector, were utilized to span the targeted $30-5000\ \mathrm{cm}^{-1}$ spectral band. In the spectral range of $30-600\ \mathrm{cm}^{-1}$, a mercury arc lamp was employed in conjunction with a 6 μm Si-coated mylar beam splitter and a liquid-helium-cooled bolometer detector. For the frequency range of $500-5000\ \mathrm{cm}^{-1}$, a globar lamp with a Ge-coated KBr beam splitter and a room-temperature DLaTGS (deuterated L-alanine doped triglycene sulphate) detector was utilized. See Fig. 1 for the merged spectra from a low-resolution survey of the transmission response at room and cryogenic temperatures. In these measurements, the silicon wafer's channel spectra were intentionally unresolved by the $\simeq 1\ \mathrm{cm}^{-1}$ instrument resolution to provide insight into the material's absorption features.

The silicon forms a Fabry–Perot etalon whose channel spectra envelope and fringe rate are set, respectively, by the impedance contrast between vacuum and the faces of sample and the phase delay in the media. With a detailed knowledge of the sample thickness, an absolute measurement of the material's dielectric properties can be realized [24]. With this end purpose in mind, additional FTS measurements were taken with a spectral resolution of $3.8 \times 10^{-3}\ \mathrm{cm}^{-1}$ in order to fully resolve fringes in the silicon etalon. Manifacier *et al.* [25] demonstrate the use of the minimum and maximum channel spectrum amplitude to determine explicitly the refractive index and sample thickness with high accuracy as a function of frequency in the limit of weak dispersion and high contrast. This alternative perspective provides insight into the accuracy and consistency of the derived physical parameters from the measured transmittance spectra.

The classical Drude–Lorentz dispersion model [26] provides useful physical insight into the infrared response of silicon's relative dielectric function:

0146-9592/20/174935-04 Journal

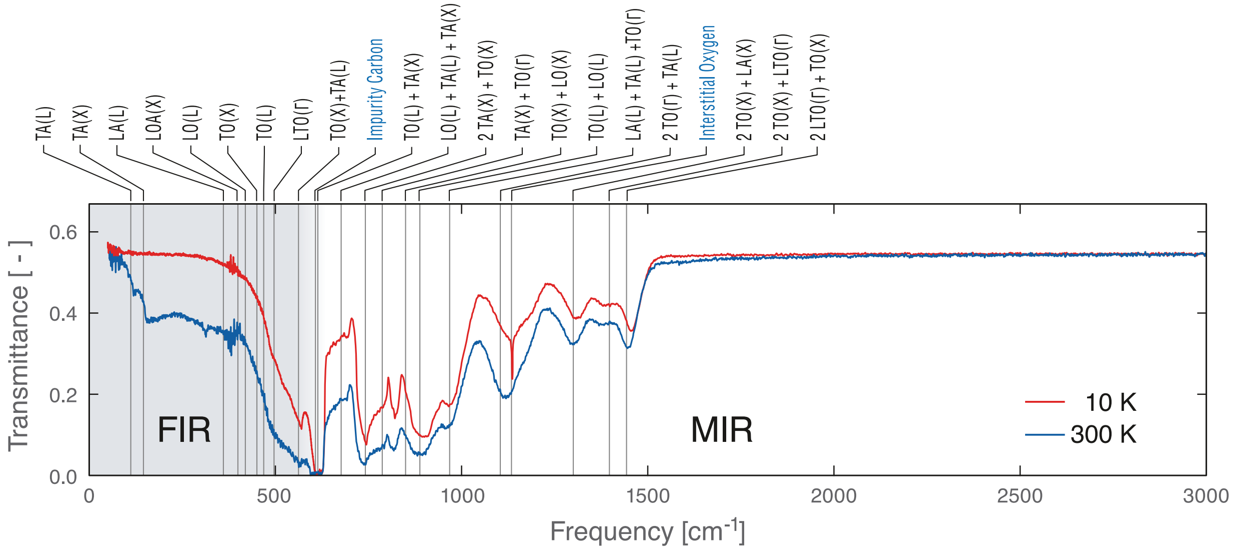

Fig. 1. Silicon etalon transmission response was characterized with a spectral resolution of $\simeq 1\ \mathrm{cm}^{-1}$ at room (blue line) and cryogenic (red line) temperatures. The transmittance, a dimensionless ratio of the sample transmission relative to a reference measurement in the absence of the sample, of an unresolved lossless etalon with a refractive index 3.4 is ≈ 0.54 [18]. The spectral range of the far- and mid-infrared FTS measurement configurations are indicated by gray and unshaded regions. The signal-to-noise ratio is degraded in the vicinity of $\approx 400\ \mathrm{cm}^{-1}$ due to an internal FTS beam splitter resonance. To facilitate identification of observable absorption features in the transmittance, the carbon impurity, interstitial [Si-O] anti-stretch [19], and phonon absorption band assignments [20–23] for silicon are adopted and displayed with annotated gray vertical lines.

$$\hat{\varepsilon}_r(\omega) = \hat{\varepsilon}_\infty - \frac{\omega_p^2}{\omega\,(\omega + i\Gamma)} + \sum_j \frac{\Delta\varepsilon_j\,\omega_j^2}{\omega_j^2 - \omega^2 - i\omega\Gamma_j}, \qquad (1)$$

where the angular frequency of the incident radiation is ω, the contribution to the permittivity from transition energies beyond the infrared is specified by $\hat{\varepsilon}_\infty$, and MKS units are adopted. The Drude term in the dielectric function accounts for free carrier conduction through the plasma frequency, ω_p, and scattering rate, Γ. The plasma frequency is defined in terms of the carrier density, $\mathcal{N}$, as follows: $\omega_p^2 = \mathcal{N} e^2 / m\varepsilon_\circ$, where e is the electron charge, m is its effective mass, and $\varepsilon_\circ = 8.854 \times 10^{-12}\mathrm{F/m}$ is the permittivity of free space. To lowest order, the plasma frequency and the scattering rate are related by $\omega_p^2 = \Gamma/\varepsilon_\circ\rho$, where ρ is the sample's bulk resistivity [27]. A sum of discrete Lorentzian terms in the dielectric function parameterizes lattice excitations in the crystal media through the oscillator strength $\Delta\varepsilon_j$, center frequency ω_j, and damping rate Γ_j for each line.

For low-loss materials, the complex refractive index, $\hat{n} = n + i\kappa$, is the preferred parameterization to mitigate contamination of the imaginary component of the dielectric function [28]. The real and imaginary components of $\hat{n}$ are related to the relative dielectric function by

$$\hat{\varepsilon}_r = \varepsilon_r' + i\varepsilon_r'' = \hat{n}^2 = (n^2 - \kappa^2) + i2n\kappa, \qquad (2)$$

where a nonmagnetic relative permeability $\hat{\mu}_r = 1$ is adopted in fully specifying the dielectric medium's electromagnetic constituent relations.

The frequency spacing, $\Delta\nu$, between consecutive spectral fringes is related to the index of refraction by $n(\nu) = m/2d\Delta\nu$, where d is the physical thickness of the etalon, and the integer m is the fringe index. Although both the fringe rate and the channel spectrum amplitude provide information regarding the etalon's transmission response, the former is significantly known more precisely in fully resolved calibrated FTS spectra. As a result, uncertainties in the sample thickness directly limit the precision of the determination of $\hat{n}$ with this methodology. The silicon etalon length was characterized at room temperature and corrected for thermal contraction through the coefficient of thermal expansion values found in Table II of Lyon *et al.* [29]. A fractional change in length of $-2.1(2) \times 10^{-4}$ upon cooling to 10 K was computed and used in the subsequent analyses performed here.

The systematic uncertainty in the measured spectrum has contributions arising from the change in illumination between the sample and reference positions, the optical alignment of the differing FTS configurations, as well as internal reflections in the instrument leading to errors in the calibrated transmittance [30]. These effects lead to the observed peaks and troughs that extend beyond the envelope of the model channel spectra shown in Fig. 2. The resolving power is influenced by the size of the limiting stop due to the differences between the on- and off-axis illumination paths [31]. This interference dies out when the path difference exceeds $x_c = 2\pi/\Omega_F \nu_i$, where Ω_F is the solid angle of the limiting stop, and ν_i is the observing wavenumber. This effect produces a frequency-dependent distortion between the measured and actual wavenumbers, $\nu_i^c = \nu_i \cdot (1 - \Omega_F/4\pi)$. For the instrument configuration employed, this leads to a contraction of the frequency scale <0.003, and the correction is applied to the data before parameter extraction.

The simulated transmittance spectra and representative observed FTS data are shown in Fig. 2. For the data below $600\ \mathrm{cm}^{-1}$, a running average of 50 channel spectra (i.e., the average of ≈ 2000 data points or equivalently a spectral range of $7.355\ \mathrm{cm}^{-1}$) from the raw FTS measurements is used to estimate the spacing for each fringe. This approach was observed

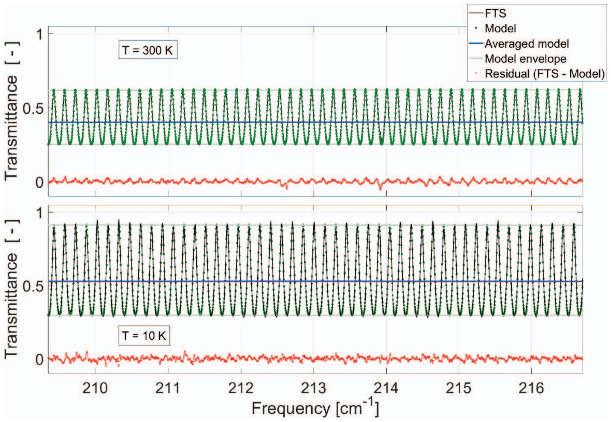

Fig. 2. Representative sample of silicon transmittance data: raw measured data (black line), high-resolution model (green points), average modeled data (blue line), and residual (raw FTS data model; red points). The gray lines indicate the envelope of the model channel spectra. For the 10 K dataset; the RMS residual error in fitting the model to the FTS data is 0.03. The RMS is reduced to 0.001 in fitting the averaged transmission model to the smoothed FTS data.

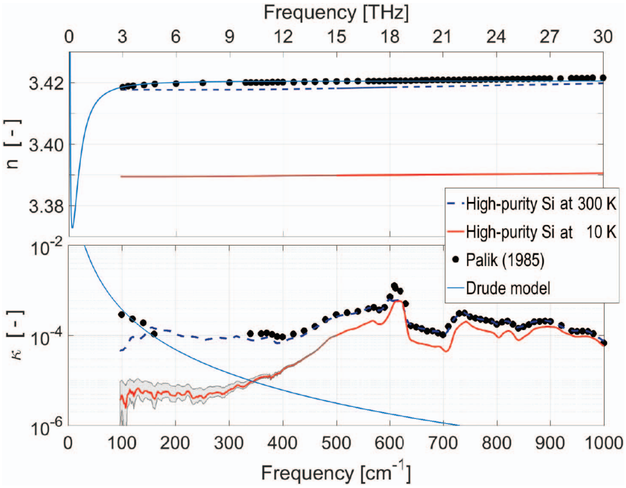

Fig. 3. Silicon's complex index of refraction: literature compilation, silicon at 300 K [35] (black symbols), measured 300 K data (blue dashed line), and measured 10 K data (red solid line). The 3σ uncertainty for the absorption index is $< 5.7 \times 10^{-6}$ (gray shaded region). A representative Drude model response (i.e., $\hat{\varepsilon}_\infty = 11.7$, $\omega_p/2\pi = 11.9\ \mathrm{cm}^{-1}$, $\Gamma/2\pi = 19.0\ \mathrm{cm}^{-1}$, $\rho = 51.0\ \Omega - \mathrm{cm}$) is indicated by blue solid lines and provides a plausible explanation for the low-frequency response in the literature data [24,35].

to reduce the sensitivity to noise and variations in the instrument response across the measurement band and is preferable to the use of adjacent peaks (or troughs) in the raw FTS measurement spectrum. The n values are then fit to a cubic spline over a $60\ \mathrm{cm}^{-1}$ spectral range, in a spirit similar to [32,33]. By design, this filtering strategy removes features at the scale of the channel spectra; however, it leaves the sample's average spectral response as a function of frequency unchanged. The imaginary component of the refractive index, κ, is extracted through a least-squares of the fit of the observed data (smoothed by a 400-point boxcar) to an averaged transmission model {Eq. (2.76); [18]}, using the real component of the refractive index as calculated above and the physical constraint $\kappa > 0$. This choice, corresponding to sampling every ≈ 10 fringes (or $1.507\ \mathrm{cm}^{-1}$), is a compromise that enables $\hat{n}$ to be recovered with improved signal-to-noise without influencing the intrinsic spectral features associated with the sample response. Imperfect FTS beam coherence induces filling of the minima and reduction of the maxima in the observed transmittance [31,34], which can potentially bias the average of the spectrum. Beam coherence factors of 0.969(2) and 0.982(0) are derived from the measured warm and cold transmittance, respectively, and are used to account for this effect in the modeled response.

The $\hat{n}$ values are subsequently regridded to a common resolution and corrected by fitting the transmission spectrum to a model that accounts for the effects of the maximum internal angle of the convergent beam in the etalon, $\beta_m = 0.872°$, using the imaginary component of the refractive index previously determined and six terms in the series of {Eq. (1); [36]}. The same cubic spline, corrected for β_m, is used to extend n above $500\ \mathrm{cm}^{-1}$, given the lack of well detectable fringes in the observed spectrum. The absorption index, κ, is derived through the same fitting approach as for the data below $600\ \mathrm{cm}^{-1}$ with a 15-point boxcar average window. The derived values for κ were blended in the overlap region $(500-600\ \mathrm{cm}^{-1})$ through a weighted average with the following weights: $w_\pm = \{1 + \tanh[\pm(\nu - \nu_\circ)/\delta\nu]\}/2$, where the central frequency of the weighting function is $\nu_\circ \approx 550\ \mathrm{cm}^{-1}$, the $\pm$ sign refers to the data above 500^{-1} and below $600\ \mathrm{cm}^{-1}$, respectively, and $\delta\nu = 20\ \mathrm{cm}^{-1}$ defines the apodization scale of the weighting function. Before blending, the κ values were characterized by a $\Delta\kappa/\kappa$ maximum offset of $\approx 5\%$ between the spectra.

For a summary of the derived refractive index, absorption index, and a comparison to prior measurements compiled from the literature [35], see Fig. 3. The change in absorption with cooling is consistent with theory and represents a factor of ≈ 2.3 reduction in κ for frequencies $<300\ \mathrm{cm}^{-1}$ relative to the highest quality material (Fig. 2.25; [37]) identified in a detailed survey of the literature. For the silicon sample explored here, the characteristic Drude response resides at frequencies below the spectral band investigated; however, the contribution of this term merits further discussion. One notes that the imaginary and real parts of the Drude response, $\varepsilon''(\Gamma) = \varepsilon_\infty - \varepsilon'(\Gamma) = \omega^2/2\Gamma^2$, are equal in magnitude at $\omega = \Gamma$, which marks the transition between the component of the dielectric function that dominates [38]. This behavior leads to the minimum in the refractive index, n, at $\omega \simeq \Gamma/2$, observed in Fig. 3. Where reported material parameters enable estimates to be computed, the position of this feature in the refractive index has been compiled for prior measurements and displayed in Fig. 4.

Impurity-induced absorption consistent with the Drude model in Czochralski silicon can be contrasted with the response of float zone silicon, which tends to exhibit weak absorption associated with the lattice band [39]. An example where the onset of this long-wavelength conductive response has been observed at ambient and frozen out (i.e., transitioned to an insulating response) at cryogenic temperatures can be found in [40]. The lack of correlation between the bulk resistivity [i.e., a feature associated with a spectral line at zero frequency as specified by the Drude term in Eq. (1)] and the observed infrared material quality [41] is anticipated from the presence of the multi-phonon lattice-band, which dominates the absorption

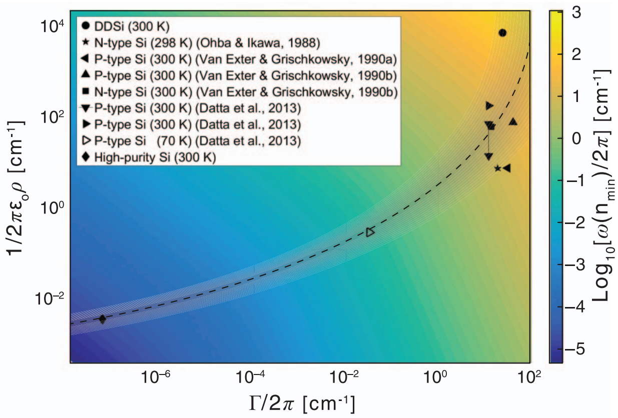

Fig. 4. Silicon Drude model summary. The minimum in the real part of the refractive index as a function of $1/\varepsilon_\circ\rho$ and Γ is presented for degenerately doped silicon (DDSi) and reported literature data [27,40,42–44]. Here, for simplicity, $\omega_p^2 = \Gamma/\varepsilon_\circ\rho$ and $\hat{\varepsilon}_\infty = 11.7$ are adopted in plotting the response. The dashed trend line and gray shaded band are provided to guide the eye.

Table 1. Silicon Refractive Index Summary at $\lambda \simeq 10$ μm

λ [μm]	$n(\lambda, 300\mathrm{K})$	$n(\lambda, T)$	$T[K]$	Ref.
10	3.4215	–		[35]
10.3	3.41551	3.38989	104	[45]
10.6	3.41765	3.38973	50	[46]
10	3.415	3.375	20	[47]
10	3.419(7)	3.390(4)	10	This work

response in the absence of free carriers [3,37]. To facilitate comparison to prior work in the short-wavelength range explored, the magnitude of the real part of the refractive index at ≈10 μm is summarized in Table 1. These observations are qualitatively consistent with prior results; however, unspecified sample composition, processing, and measurement details associated with the literature regrettably hamper a more quantitive assessment.

Funding. National Aeronautics and Space Administration (SOFIA 15-S3GSI15-2-0003); Goddard Space Flight Center (Internal Research and Development).

Acknowledgment. The authors thank B. Cabrera, B. A. Young, A. S. Kutyrev, S. H. Moseley, and R. J. Schoelkopf for sample acquisition and technical discussions. A. C. Wollack is acknowledged for contributions to algorithm development.

Disclosures. The authors declare no conflicts of interest.

REFERENCES

1. S. J. Weber, K. W. Murch, D. H. Slichter, R. Vijay, and I. Siddiqi, Appl. Phys. Lett. **98**, 172510 (2011).
2. J. W. Lamb, Int. J. Infrared Millim. Waves **17**, 1997 (1996).
3. M. N. Afsar and H. Chi, Int. J. Infrared Millim. Waves **15**, 1181 (1994).
4. J. Krupka, J. Breeze, A. Centeno, N. Alford, T. Claussen, and L. Jensen, IEEE Trans. Microw. Theory Tech. **54**, 3995 (2006).
5. G. Cataldo, E. J. Wollack, E. M. Barrentine, A. D. Brown, S. H. Moseley, and K. U-Yen, Rev. Sci. Instrum. **86**, 013103 (2015).
6. L. Ding, I. Shih, T. J. Pavlasek, and C. Champness, IEEE Trans. Microw. Theory Tech. **32**, 151 (1984).
7. V. L. Gurevich and A. K. Tagantsev, Adv. Phys. **40**, 719 (1991).
8. W. Theiss, *Optical Properties of Porous Silicon* (Elsevier, 1997).
9. K. Mallik, R. J. Falster, and P. R. Wilshaw, Semicond. Sci. Technol. **18**, 517 (2003).
10. M. Balkanski and W. Nazarewicz, J. Phys. Chem. Solids **23**, 573 (1962).
11. P. F. Ermolov, D. E. Karmanov, A. K. Leflat, V. M. Manankov, M. M. Merkin, and E. K. Shabalina, Semiconductors **36**, 1114 (2002).
12. J. Molla, R. Vila, R. Heidinger, and A. Ibarra, J. Nucl. Mater. **258**-263, 1884 (1998).
13. W. Götz, G. Pensl, and W. Zulehner, Phys. Rev. B **46**, 4312 (1992).
14. J. Cotter, J. Guo, P. Cousins, M. Abbott, F. Chen, and K. Fisher, IEEE Trans. Electron Dev. **53**, 1893 (2006).
15. R. J. Collins and H. Y. Fan, Phys. Rev. **93**, 674 (1954).
16. W. Kaiser, P. H. Keck, and C. F. Lange, Phys. Rev. **101**, 1264 (1956).
17. J. R. Aronson, H. G. McLinden, and P. J. Gielisse, Phys. Rev. **135**, A785 (1964).
18. C. F. Bohren and D. R. Huffman, *Absorption and Scattering of Light by Small Particles* (Wiley, 1983).
19. D. R. Bosomworth, W. Hayes, A. R. L. Spray, and G. D. Watkins, Proc. R. Soc. Lond. Ser. A, Math. Phys. Sci. **317**, 133 (1970).
20. J. Ihm, M. Yin, and M. L. Cohen, Solid State Commun. **37**, 491 (1981).
21. M. T. Yin and M. L. Cohen, Phys. Rev. B **26**, 3259 (1982).
22. M. T. Yin and M. L. Cohen, Phys. Rev. B **26**, 5668 (1982).
23. M. Pradhan, R. Garg, and M. Arora, Infrared Phys. **27**, 25 (1987).
24. J. Birch, Infrared Phys. **18**, 613 (1978).
25. J. C. Manifacier, J. Gasiot, and J. P. Fillard, J. Phys. E **9**, 1002 (1976).
26. F. Gervais, in Vol. **8** of *Infrared and Millimeter Waves–Electromagnetic Waves in Matter, Part I*, K. J. Button, ed. (Academic Press, 1983), pp. 284–287.
27. M. van Exter and D. Grischkowsky, Appl. Phys. Lett. **56**, 1694 (1990).
28. M. N. Afsar and K. J. Button, IEEE Trans. Microw. Theory Tech. **31**, 217 (1983).
29. K. G. Lyon, G. L. Salinger, C. A. Swenson, and G. K. White, J. Appl. Phys. **48**, 865 (1977).
30. M. R. Burleigh, C. R. Richey, S. A. Rinehart, M. A. Quijada, and E. J. Wollack, Appl. Opt. **55**, 8201 (2016).
31. J. Chamberlain, *The Principles of Interferometric Spectroscopy* (Wiley, 1979).
32. C. M. Randall and R. D. Rawcliffe, Appl. Opt. **6**, 1889 (1967).
33. D. F. Edwards and E. Ochoa, Appl. Opt. **19**, 4130 (1980).
34. E. N. Grossman and D. G. McDonald, Opt. Eng. **34**, 1289 (1995).
35. E. Palik, *Handbook of Optical Constants of Solids* (Elsevier, 1998).
36. D. Chandler-Horowitz and P. M. Amirtharaj, J. Appl. Phys. **97**, 123526 (2005).
37. P. Bruesch, *Phonons: Theory and Experiments II* (Springer-Verlag, 1987), pp. 51–58.
38. M. Ordal, L. Long, R. Bell, S. Bell, R. Bell, R. Alexander, and C. Ward, Appl. Opt. **22**, 1099 (1983).
39. T. Ohba and S.-I. Ikawa, J. Appl. Phys. **64**, 4141 (1988).
40. R. Datta, C. D. Munson, M. D. Niemack, J. J. McMahon, J. Britton, E. J. Wollack, J. Beall, M. J. Devlin, J. Fowler, P. Gallardo, J. Hubmayr, K. Irwin, L. Newburgh, J. P. Nibarger, L. Page, M. A. Quijada, B. L. Schmitt, S. T. Staggs, R. Thornton, and L. Zhang, Appl. Opt. **52**, 8747 (2013).
41. P. W. Collyer, Appl. Opt. **5**, 765 (1966).
42. R. T. Kinasewitz and B. Senitzky, J. Appl. Phys. **54**, 3394 (1983).
43. M. van Exter and D. Grischkowsky, Phys. Rev. B **41**, 12140 (1990).
44. S. Nashima, O. Morikawa, K. Takata, and M. Hangyo, J. Appl. Phys. **90**, 837 (2001).
45. W. L. Wolfe, A. G. DeBell, and J. M. Palmer, Proc. SPIE **0245**, 164 (1980).
46. J. M. Hoffman and W. L. Wolfe, Appl. Opt. **30**, 4014 (1991).
47. G. Hawkins and R. Hunneman, Infrared Phys. Technol. **45**, 69 (2004).